A two degree-of-freedom linear vibration energy harvester for tram applications

M. Perez, S. Chesné, C. Jean-Mistral, K. Billon, R. Augez, C. Clerc

A two degree-of-freedom linear vibration energy harvester for tram applications

M. Perez[1], S. Chesné[1], C. Jean-Mistral[1], K. Billon[1], R. Augez[2] and C. Clerc[2]

[1] Université de Lyon, CNRS INSA-Lyon, LaMCoS UMR5259, Avenue Jean Capelle, F-69261 Villeurbanne, France
[2] Vibratec, 28 chemin du petit bois, F-69130 Ecully, France

E-mail: simon.chesne@insa-lyon.fr

Abstract. This paper presents an innovative two degree-of-freedom (DoF) electromagnetic vibration energy harvester used in a railway environment and its optimization based on complete multi-physics modeling, coupling an analytical model, numerical magnetic flied simulations and experimental data used as input parameters. It highlights that the resonance frequencies of the harvester must not be equal to the predominant frequencies of the input signal, which differs greatly compared to the optimization of a one DoF device. Characteristic frequency hopping dependent on the mechanical quality factors linked to the two DoF is also observed. Two prototypes were designed and tested with real tram acceleration signals. An average electrical power of 6.5mW was obtained experimentally with a prototype of 710 grams and 141 cubic centimeters, validating the multi-physics model and the optimization process.

Keywords. Vibration energy harvesting, electromagnetic conversion, permanent magnets, inertial linear generator, structural health monitoring

Introduction

Increasing the lifetime of railway structures and improving the safety and comfort for all passengers are two major issues for the railway industry. Over the past few decades, Structural Health Monitoring (SHM) has been used to detect and monitor faults in railway structures, with the final aim to act preventively, which could lead to significant economic gains and much lower maintenance periods. SHM involves the development of a network able to sense and communicate on the health of the structure, and requires an energy supply for each node of the network. A promising alternative could be the development of autonomous sensing nodes able to harvest energy from their surroundings. In this context, a wide range of vibration energy harvesters have been developed specifically for the railway industry. Many devices convert the linear displacement of the track into a rotary motion using racks and pinions [1-10], endless screws [11], pistons [12] or cams and pinions [13-14], to supply an electromagnetic motor operating as an alternator. The electrical power produced with these bulky and heavy systems is very high (32-150W), but for very short time periods: a few seconds for each passing train. On the other hand, simple piezoelectric patches directly attached to the structure scavenge very low levels of power (53-110µW) [15-17]. Finally, many inertial devices embedded in trains have been developed [18-30]. Park *et al.* proposed a one degree-of-freedom (DoF) system consisting of a clamped-free beam with permanent magnets, able to scavenge up to 1.19mW at 51.5Hz with a compact size of 8.8 x 5.4 x 4.7 cm^3, and weighing under 1g [27]. De Pasquale designed a one DoF device based on magnetic levitation dedicated to low frequency bandwidths (3-5Hz) [21]. Also, based on magnetic levitation, Gao *et al.* developed a one DoF system that could scavenge 5.56mW for 3-7Hz frequencies [29]. All these systems scavenge enough energy to supply a sensor node but remain fragile and their performances are based on sinusoidal excitations. For SHM applications, an average electrical power between 1 and 10mW must be harvested from the surrounding in order to supply the sensors node. This power depends on the sensor used (accelerometer, temperature sensor, GPS sensor…), on the

measurement sampling (1 measure each 30s or 1 measure each hour), on the embedded electronic and intelligence (simply read the measurement or compute a performance index) and depends on the communication process chosen (ZigBee…). The measurement strategy (sleep, wake-up, measure, compute, transmit) and the average consumption of the node must be optimized to match the available harvested electrical power.

For railway applications, on-board systems seem a valid solution to supply sensors used for mapping railway structures with a single device. The harvester must be able to operate in the harsh environment of railways (dust, moisture, lubricant) and be robust in order to sustain high levels of acceleration (up to 10g). This has led to the development of compact encapsulated inertial devices based on electromagnetic conversion. Perpetuum commercializes a one DoF electromagnetic harvester for which the resonance frequency can be tuned to match the entrance spectrum of vibration (from 25 up to 120Hz). Their system can handle high levels of acceleration (up to 4.91g) and harvest 27.5mW. Revive also propose a tunable electromagnetic system (resonant frequency from 15Hz up to 100Hz) with high performances in term of energy scavenging (up to 150mW for ModelA). These robust embedded electromagnetic inertial devices are one DoF systems with a resonance frequency tuned in accordance with the more relevant frequency of the input spectrum of vibration. Nevertheless, the input spectrum of vibration induced on a train or a tram is very complex, with more than one predominant frequency.

Electromagnetic harvesters are well-known and various models have been developed in the literature for one DoF linear [31] and non-linear devices [32] and for two or more DoF devices [33-34]. But most of the models and structure designs proposed have been tested and validated under sinusoidal excitation, which remains very far from real signal excitations (noise, shock, complex excitations). In addition, they are based on classical hypotheses such as the omission of internal electric losses, no edge effects, etc. Here, we propose to design a two DoF electromagnetic vibration energy harvester able to provide the required power levels (1-10mW) and we present a method for efficiently optimizing the parameters of a two DoF electromagnetic harvester under real complex mechanical stimulation for railway applications. Our analytical/numerical model takes into account all the contributions generally neglected such as internal losses, and is easily tunable and adaptable to any kind of input vibration spectrum. This paper is divided into three sections to describe the different steps of resolution represented in Figure 1.

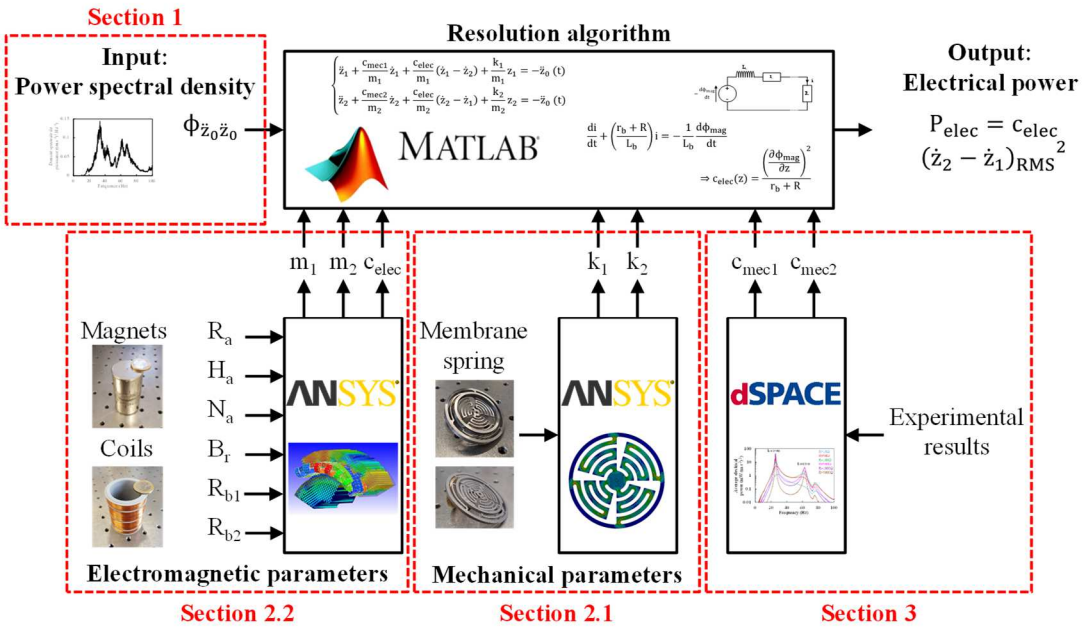

Figure 1: Block diagram representing the different steps of optimization.

The first section will describe the vibratory environment of the tram and especially the power spectral density measured on the bogie, which will provide the basis of our optimization. Section 2.1 will be devoted to the analysis and optimization of a two degree-of-freedom inertial device which appears very

attractive for railway applications in comparison to one DoF devices. Section 2.2 will outline the equations associated with the electromagnetic conversion and the optimization based on FEM calculations. Finally, section 3 will introduce the experimental results obtained with a two DoF electromagnetic device.

1. Vibratory environment of a tram

In view to effectively detecting overall potential defects, which primarily concern the rails and the lower part of the tram, the harvester will be located near the sensors used, namely on the bogie (Figure 2). In order to clearly determine the vibratory environment of the bogie in operation, two series of field measurements were conducted, in 2017 and 2018, respectively. During these tests, three piezoelectric charge accelerometers (B&K type 4393) were placed on a Citadis® 402 bogie, to measure the vertical acceleration $\ddot{z}_0(t)$ during trips on the railway network of Lyon (Figure 2). This redundancy of acceleration measurement was to prevent eventual failures of one of the sensors, which is often the case in in-situ measurements, but also necessary to check the dispersion of the measurements. A total of 179 measurements were performed, equivalent to almost five hours of data, with a very good correlation between the three sensors (a few percents).

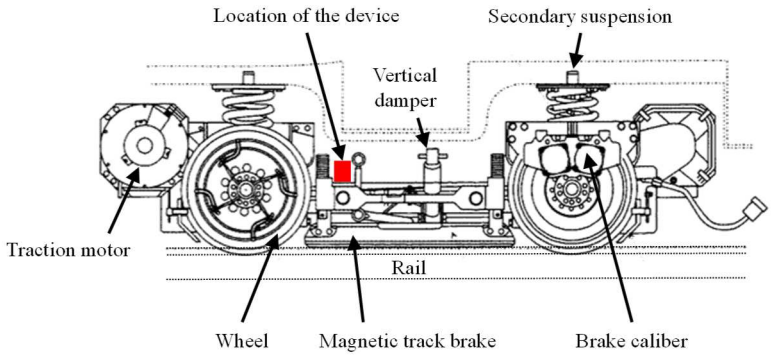

Figure 2: Side view of an Arpege™ bogie used on the Citadis® 402 tram.

Figure 3a shows the instantaneous acceleration measured on the bogie during five consecutive trips (from one station to the next one) in Lyon. It should be noted that the acceleration can reach peak-to-peak values of ±100m.s^{-2} for an RMS value of approximately 5m.s^{-2} on the entire network. Classically, electromagnetic harvesters are designed for large input displacements in order to maximize the variation of fluxes between the coils and the permanent magnets.

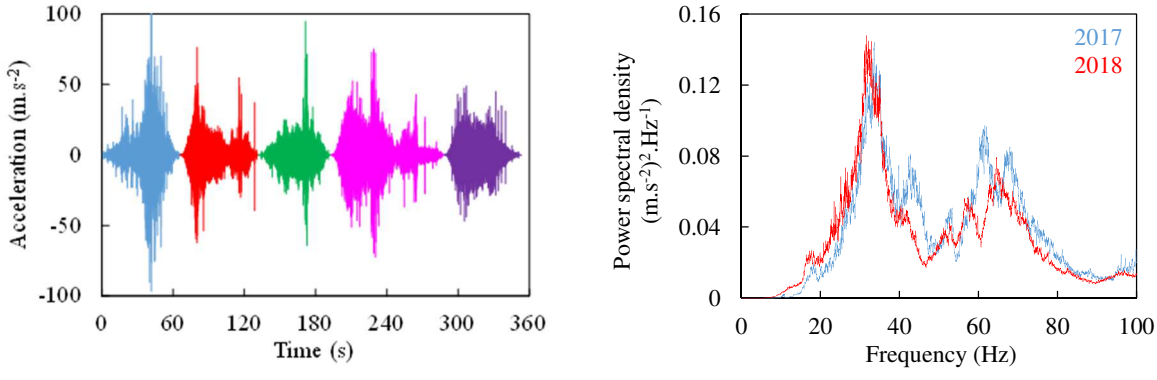

Figure 3: (a) Example of acceleration levels during five trips. (b) PSD averaged over all the trips made in 2017 and 2018 on two different trams.

The Power Spectral Density (PSD) averaged over the 179 trips made in 2017 and 2018 demonstrated very good repeatability regarding the two first predominant frequencies (<2Hz), with a one-year interval and two different Citadis® 402 trams (Figure 3b). However, it is true that these small differences could modify slightly the optimization of our harvester. In order to develop an efficient harvester useful for

several lines of tramway, it would have been necessary to average the PSD associated to each vehicle used in Lyon, which remains a quite long and fastidious measurement campaign. The vibratory environment of the Citadis® 402 on the Lyon network is characterized by wide band behavior, with two predominant frequencies at $f_1 \approx 33$Hz and $f_2 \approx 62$Hz. This vibration spectrum was used as a mechanical input signal for our new harvester, justifying the design of a two DoF system.

2. Modeling and numerical optimization

2.1 Mechanical modeling of the two DoF linear system

Figure 4a illustrates the two degree-of-freedom (DoF) inertial energy harvester considered to scavenge energy on the tram bogie composed of an outer frame attached to the bogie, two masses m_1 and m_2 which are able to move inside the outer frame thanks to two linear springs of stiffnesses k_1 and k_2. All the mechanical losses (spring heating, friction in the air, etc.) are modeled by two linear dampings c_{mec1} and c_{mec2}. An electromagnetic converter basically requires two components in relative motion to produce electrical power: an inductor composed of permanent magnets (with a mass m_1) and an armature composed of coils (with a mass m_2). In our device, the two mechanical DoFs are set in parallel (Figure 4a), which differs from the other devices of the state of the art in which the coils are fixed, leading to a one DoF device (Figure 4b). The electromechanical coupling describing the harvesting process is modeled by linear electrical damping c_{elec} related to the relative speed between the two masses (section 2.2).

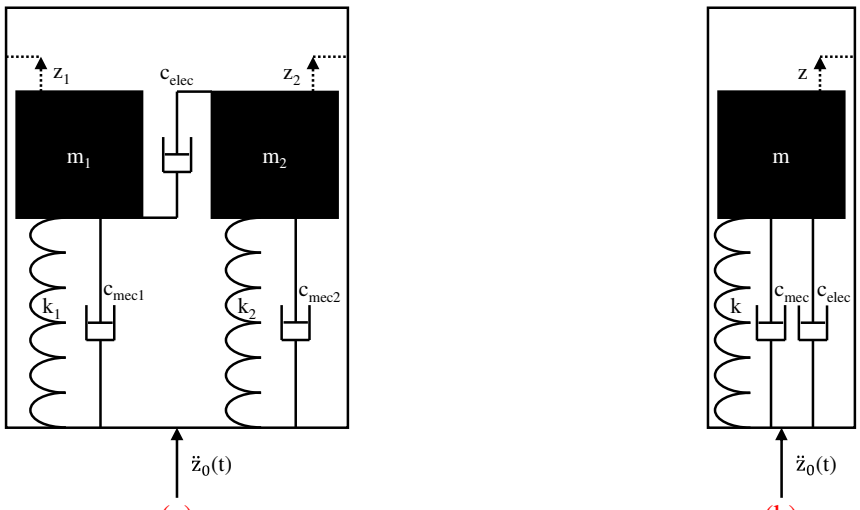

Figure 4: Schematic representation of: (a) a 2 DoF system and (b) a 1 DoF system.

As the bogie vibrates with acceleration $\ddot{z}_0(t)$, Newton's second law of motion allows us to write the following equation (1):

$$\begin{cases} \ddot{z}_1 + \dfrac{\omega_{01}}{Q_1}\dot{z}_1 + \dfrac{c_{elec}}{m_1}(\dot{z}_1 - \dot{z}_2) + \omega_{01}^2 z_1 = -\ddot{z}_0(t) \\ \ddot{z}_2 + \dfrac{\omega_{02}}{Q_2}\dot{z}_2 + \dfrac{c_{elec}}{m_2}(\dot{z}_2 - \dot{z}_1) + \omega_{02}^2 z_2 = -\ddot{z}_0(t) \end{cases} \quad (1)$$

With z_i being the relative displacement of each mass m_i from its equilibrium position and $Q_i = \dfrac{\sqrt{k_i m_i}}{c_{meci}}$ the mechanical quality factor associated with each degree of freedom. The harvester therefore has two natural angular frequencies associated with each degree of freedom: $\omega_{01} = \sqrt{\dfrac{k_1}{m_1}} = 2\pi f_{01}$ and $\omega_{02} = \sqrt{\dfrac{k_2}{m_2}} = 2\pi f_{02}$. In the Fourier frequency domain, the transfer function of the system H(jω) is defined as the ratio between the output positions $Z = \begin{bmatrix} z_1 \\ z_2 \end{bmatrix}$ and the input acceleration $\ddot{Z}_0 = \begin{bmatrix} \ddot{z}_0 \\ \ddot{z}_0 \end{bmatrix}$:

$$H(j\omega) = \frac{Z}{\ddot{Z}_0} = \begin{bmatrix} H_{11} = \omega^2 - {\omega_{01}}^2 - j\left(\frac{\omega_{01}}{Q_1} + \frac{c_{elec}}{m_1}\right)\omega & H_{12} = j\frac{c_{elec}}{m_1}\omega \\ H_{21} = j\frac{c_{elec}}{m_2}\omega & H_{22} = \omega^2 - {\omega_{02}}^2 - j\left(\frac{\omega_{02}}{Q_2} + \frac{c_{elec}}{m_2}\right)\omega \end{bmatrix}^{-1} \quad (2)$$

The power spectral density (PSD) of the output relative displacements between the two masses $\Delta z = z_2 - z_1$ can be expressed as a function of the PSD of the input acceleration $\phi_{\ddot{z}_0\ddot{z}_0}(j\omega)$ thanks to the transfer function $H(j\omega)$ [35].

$$\phi_{\Delta z \Delta z}(j\omega) = |H_{21} + H_{22} - H_{11} - H_{12}|^2 \times \phi_{\ddot{z}_0\ddot{z}_0}(j\omega) \quad (3)$$

In this respect, the average RMS relative speed between the two masses can be calculated from the PSD $\phi_{\Delta z \Delta z}(j\omega)$ by performing a simple calculation of integrals:

$$\Delta\dot{z}_{RMS} = (\dot{z}_2 - \dot{z}_1)_{RMS} = \sqrt{\frac{1}{2\pi}\int_0^\infty \omega^2 \phi_{\Delta z \Delta z}(j\omega)d\omega} \quad (4)$$

Finally, the average output electric power is given by equation (5).

$$P_{elec} = c_{elec} \times {\Delta\dot{z}_{RMS}}^2 \quad (5)$$

The optimization of our two DoF electromagnetic transducer is therefore based on a spectral resolution (equations (2) to (5)) using the PSD of the acceleration measured on the tram (Figure 3) as the input mechanical signal. A parametric study based on the resolution of the temporal equations (1) would be too long as the input temporal signal represents hours of measurements. The aim of our optimization is to maximize the electrical power P_{elec} by selecting the correct resonance frequencies (f_{01} and f_{02}) and electrical damping c_{elec} values of our transducer. In what follows, the optimal resonance frequencies and electrical damping values will be the values that allow maximizing the electrical power harvested.

Figure 5 shows the average electrical power depending on the first resonance frequency f_{01} and the second resonance frequency f_{02} when considering the real excitation of the tram (PSD based on the 179 trips mentioned previously). The simple case chosen ($m_1=m_2$, $Q=Q_1=Q_2$) highlights certain major results of the resonance frequency values as a function of the mechanical quality factor Q. Four mechanical quality factors from 5 to 100, which is a typical range of what can be achieved experimentally, were tested. It might have been expected that the optimal first resonance frequency f_{01} would be very close to f_1 =33Hz and the optimal second resonance frequency f_{02} would be very close to f_2=62Hz, since these frequencies are the two predominant frequencies of the input signal (Figure 3b). The results obtained by our parametric study demonstrate that this is not at all so in reality. In fact, to increase the electrical power P_{elec}, the relative velocity between m_1 and m_2 must be maximized which can be achieved in two ways: (i) by generating a large phase difference between the 2 DoF even if the amplitude is low, or (ii) by enabling large amplitudes with low phase differences.

The first strategy can be seen in Figure 5, with the hypothetical case where one of the resonance frequencies is equal to zero (unachievable in practice) while the other resonance frequency is set from 48Hz to 50Hz. In this case, the two resonance frequencies are sufficiently separated to obtain a large phase difference between the two DoFs over a broad frequency range, and especially around the first predominant frequency f_1. This optimization strategy is the same regardless of the mechanical quality factors. Nevertheless, as the displacement of each DoF is very small, a high electrical damping value c_{elec} is required to maximize the electrical power, which is not always possible in practice.

(a)

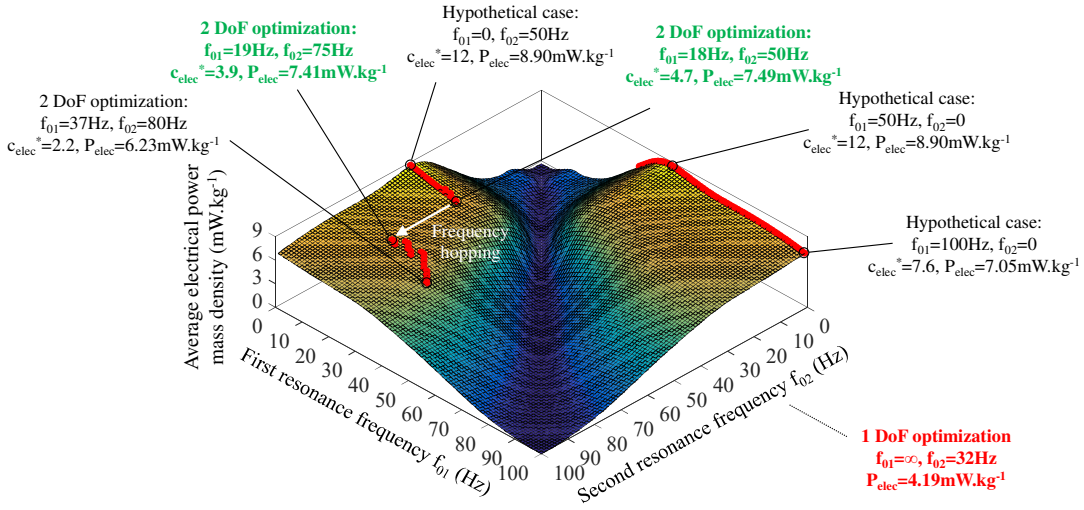
2 DoF optimization:
f01=19Hz, f02=75Hz
celec*=3.9, Pelec=7.41mW.kg-1
Hypothetical case:
f01=0, f02=50Hz
celec*=12, Pelec=8.90mW.kg-1
2 DoF optimization:
f01=18Hz, f02=50Hz
celec*=4.7, Pelec=7.49mW.kg-1
2 DoF optimization:
f01=37Hz, f02=80Hz
celec*=2.2, Pelec=6.23mW.kg-1
Hypothetical case:
f01=50Hz, f02=0
celec*=12, Pelec=8.90mW.kg-1
Hypothetical case:
f01=100Hz, f02=0
celec*=7.6, Pelec=7.05mW.kg-1
Frequency hopping
Average electrical power mass density (mW.kg-1)
First resonance frequency f01 (Hz)
Second resonance frequency f02 (Hz)
1 DoF optimization
f01=∞, f02=32Hz
Pelec=4.19mW.kg-1

(b)

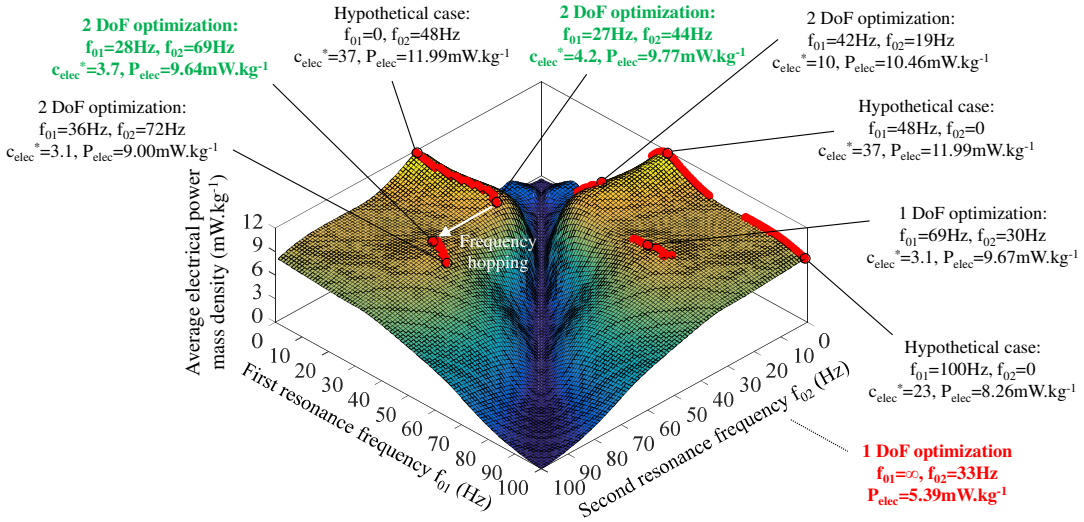
2 DoF optimization:
f01=28Hz, f02=69Hz
celec*=3.7, Pelec=9.64mW.kg-1
Hypothetical case:
f01=0, f02=48Hz
celec*=37, Pelec=11.99mW.kg-1
2 DoF optimization:
f01=27Hz, f02=44Hz
celec*=4.2, Pelec=9.77mW.kg-1
2 DoF optimization:
f01=42Hz, f02=19Hz
celec*=10, Pelec=10.46mW.kg-1
2 DoF optimization:
f01=36Hz, f02=72Hz
celec*=3.1, Pelec=9.00mW.kg-1
Hypothetical case:
f01=48Hz, f02=0
celec*=37, Pelec=11.99mW.kg-1
1 DoF optimization:
f01=69Hz, f02=30Hz
celec*=3.1, Pelec=9.67mW.kg-1
Frequency hopping
Hypothetical case:
f01=100Hz, f02=0
celec*=23, Pelec=8.26mW.kg-1
Average electrical power mass density (mW.kg-1)
First resonance frequency f01 (Hz)
Second resonance frequency f02 (Hz)
1 DoF optimization
f01=∞, f02=33Hz
Pelec=5.39mW.kg-1

(c)

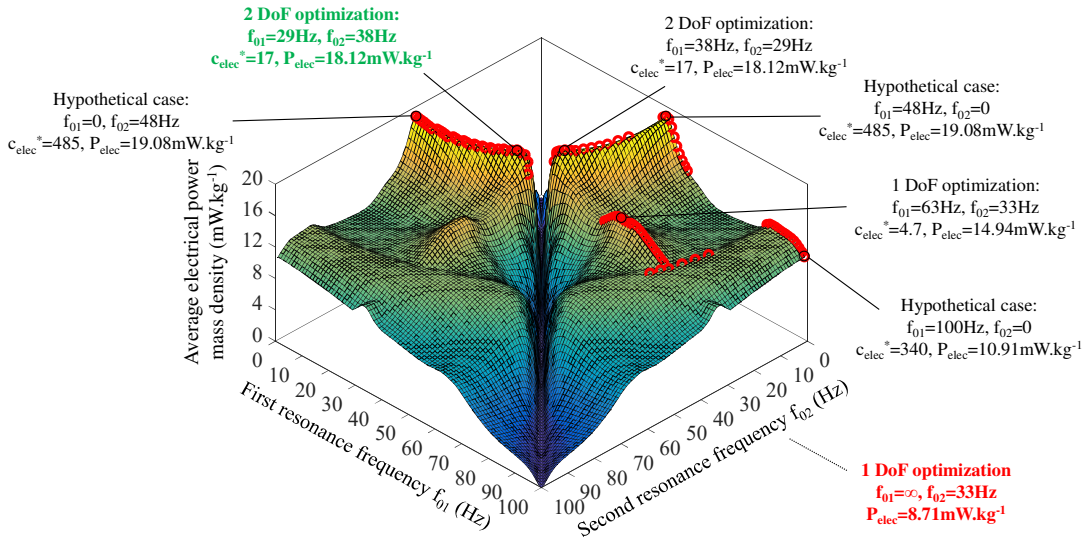
2 DoF optimization:
f01=29Hz, f02=38Hz
celec*=17, Pelec=18.12mW.kg-1
2 DoF optimization:
f01=38Hz, f02=29Hz
celec*=17, Pelec=18.12mW.kg-1
Hypothetical case:
f01=0, f02=48Hz
celec*=485, Pelec=19.08mW.kg-1
Hypothetical case:
f01=48Hz, f02=0
celec*=485, Pelec=19.08mW.kg-1
1 DoF optimization:
f01=63Hz, f02=33Hz
celec*=4.7, Pelec=14.94mW.kg-1
Hypothetical case:
f01=100Hz, f02=0
celec*=340, Pelec=10.91mW.kg-1
Average electrical power mass density (mW.kg-1)
First resonance frequency f01 (Hz)
Second resonance frequency f02 (Hz)
1 DoF optimization
f01=∞, f02=33Hz
Pelec=8.71mW.kg-1

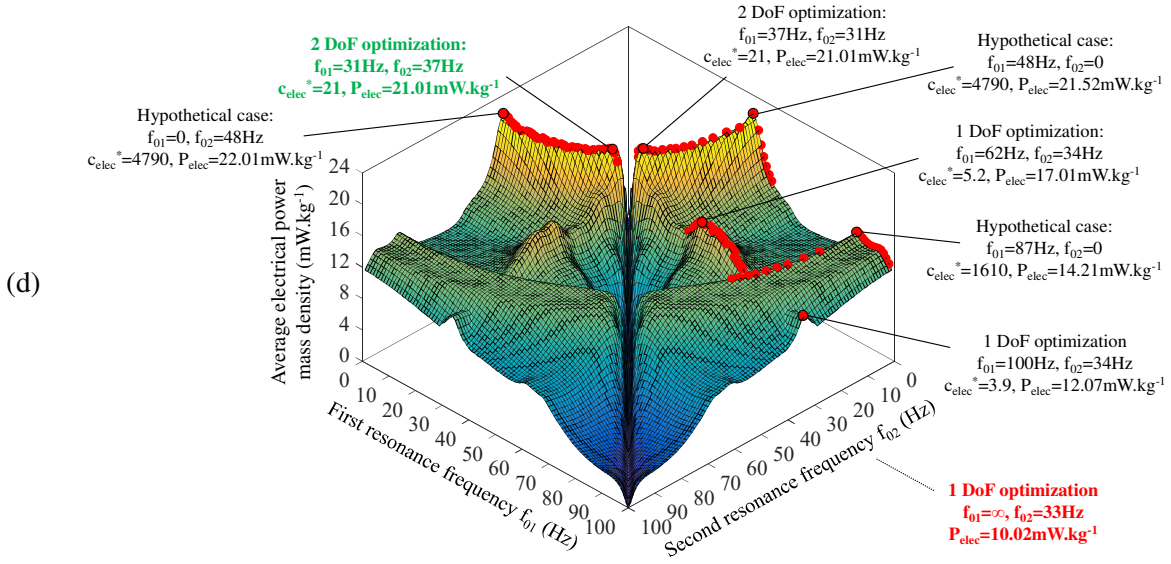

Figure 5: Average electrical power mass density $\frac{P_{elec}}{m_1+m_2}$ depending on the first and second resonance frequencies (with the optimal electrical damping, $m_1=m_2$, $Q=Q_1=Q_2$): (a) Q=5, (b) Q=10, (c) Q=50, (d) Q=100. The red circles represent the local maximums for each value of f_{01}.

Figure 5 shows that the second resonance frequency f_{02} decreases as the first resonance frequency f_{01} increases in order to reach the second strategy where the two resonance frequencies tend to be very close to each other. Regarding this, the amplitudes of displacement of the two DoF are increased but the phase difference between the two DoF is reduced. Figure 6a shows an example of this strategy where f_{01} is set to 28Hz and f_{02} is set to 37.6Hz for Q=50. It can be seen that for a high mechanical quality factor, the passage of the resonance of each DoF is fast and sharp enough for the second strategy to be applied. Thus, it is pertinent to say that the two resonance frequencies f_{01} and f_{02} are tuned to exploit the first dominant frequency of bogie f_1.

For the lowest mechanical quality factor, the first strategy, i.e. that of promoting a large phase shift, is preferred as frequency hopping emerges above a certain value of f_{01} (Figure 5a and Figure 5b). Indeed, for a low mechanical quality factor, the amplitude of the displacement of each DoF is low even at the resonance, and thus not sufficient to offset a low phase shift. The condition of the second strategy is not respected. Figure 6b illustrates an example for a mechanical quality factor of 5. In this case, it is interesting to select f_{02} just beyond f_2, as shown in Figure 5. A large phase difference can therefore be obtained while having significant amplitudes. Thus, for our two DoF transducer with a low quality factor, the optimum value of the first resonance frequency f_{01} remains close to the first predominant frequency f_1 while f_{02} ranges from 67Hz to 77Hz. In this case, the first resonance frequency f_{01} is therefore tuned to exploit the first dominant frequency of the bogie f_1 while the second resonance frequency f_{02} is tuned to exploit the second dominant frequency of the bogie f_2.

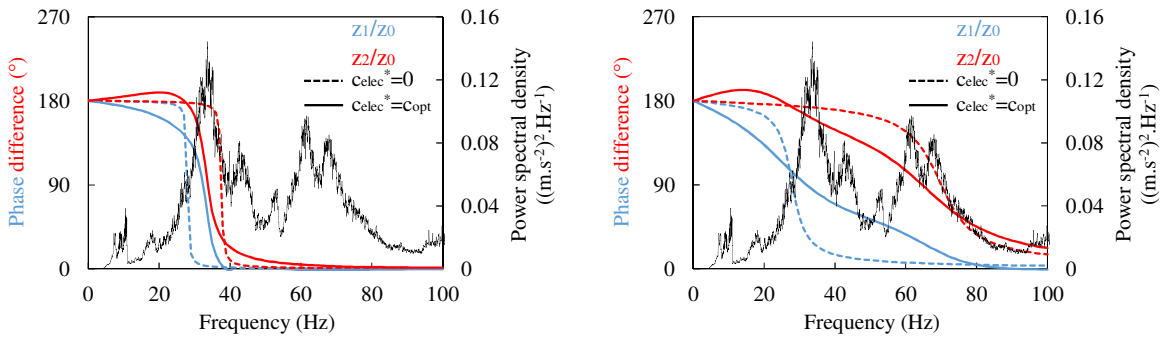

Figure 6: Illustration of the phase difference of the two masses: (a) $Q=Q_1=Q_2=50$, $f_{01}=28$Hz, $f_{02}=37.6$Hz, (b) $Q=Q_1=Q_2=5$, $f_{01}=28$Hz, $f_{02}=72.4$Hz.

It can be seen in Figure 5 that varying the first resonance frequency does not significantly impact the electric power mass density produced for $0 \leq f_{01} \leq 30$Hz, if f_{02} is well-tuned. For railway applications, the harvester must sustain high accelerations (up to 10g) which induces technological constraints, especially for the design and stiffness of the springs used. Moreover, as mentioned previously, achieving high electrical damping c_{elec} can be difficult in practice, since the electric damping value is limited by technology (see section 2.2). For these practical reasons, the decision was taken to restrict the first resonance frequency f_{01} of our two DoF transducer to between 26Hz and 30Hz. Finally, Figure 5 also introduces the optimal electrical damping c_{elec}^* on several points. It demonstrates that the optimal electrical damping must always be greater than 1 (i.e. $c_{elec} > c_{mec}$) and its value increases with the mechanical quality factors, as is generally the case for broadband excitations [34]. Figure 7 summarizes the optimal frequencies for high and low mechanical quality factors.

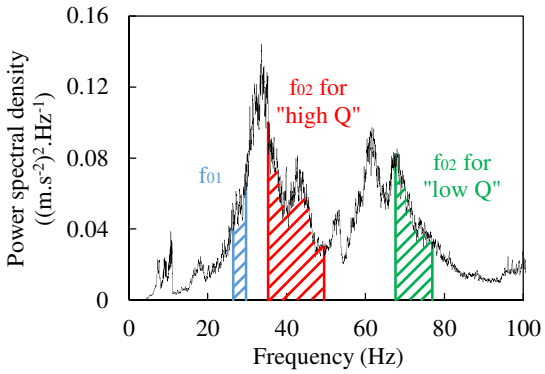

Figure 7: Representation of the optimal resonance frequencies on the PSD.

In order to understand the real contribution of these results, let us introduce the single DoF linear system, which is in fact equivalent to a 2 DoF system with one of the resonance frequencies set to a very high value ($f_{01}=\infty$ for example). With our experimental input PSD, Figure 8a shows the average electrical power mass density (P_{elec}/m) depending on the resonance frequency of a single DoF linear system for different mechanical quality factors. In this case, the parametric optimization highlights that the resonant frequency of the one DoF harvester must be close to the first predominant frequency ($f_1 \approx 33$Hz) of the input mechanical solicitation, in order to maximize the scavenged energy. The electrical power P_{elec} is still proportional to the moving mass (m) but no longer to the mechanical quality factor (Q). It is therefore less interesting to obtain high mechanical quality factors in comparison with a sinusoidal excitation. In addition, Figure 8b indicates that the optimal electrical damping c_{elec} must always be greater than c_{mec}, especially for high mechanical quality factors ($c_{elec}^*=2.7$ at Q=5, $c_{elec}^*=2.8$ at Q=10, $c_{elec}^*=4.3$ at Q=50, $c_{elec}^*=5.7$ at Q=100. This behavior is similar to that obtained for our two DoF electromagnetic transducer.

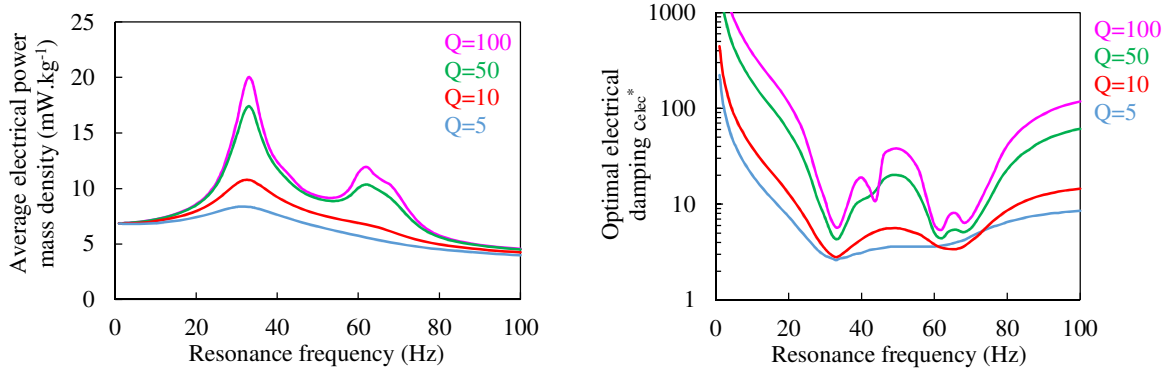

Figure 8: Comparison to a 1 DoF energy harvester: (a) Illustration of the average electrical power mass density $\frac{P_{elec}}{m}$ depending on the resonance frequency f_0 of the system (with the optimal electrical damping). (b) Illustration of the dimensionless optimal electrical damping $\left(c_{elec}^* = \frac{c_{elec}}{c_{mec}}\right)$.

It can therefore be established that a one DoF is very simple to optimize since it is sufficient to select a resonance frequency f_0 close to $f_1 \approx 33$Hz once the mechanical quality factor is rather high. The optimization of a two DoF is more complicated as the first resonance frequency f_{01} must be selected slightly lower than f_1=33Hz while the second resonance frequency f_{02} is highly dependent on the mechanical quality factor and the electrical damping, as underlined previously (Figure 5). Finally, the optimal electrical damping is very high in both cases. However, high electrical damping can only be obtained with an armature whose mass (m_2) is significant compared to the mass of the inductor (m_1), hence the benefit of adding a second DoF to take advantage of the inertia of m_2.

2.2 Electromagnetic modeling

As underlined previously, the optimal value of the electrical damping c_{elec} must be high to maximize the output electric power P_{elec}. The electrical damping in our transducer results from the coupling between moving magnets and fixed coils, a configuration more appropriate for inertial systems and which enables strong electrical damping. Generally, such converters are modeled electrically by a voltage source in series with the inductance L_b and the resistance r_b of the coils (Figure 9). The value of the electrical voltage is given by the Faraday's law equal to the temporal variation of magnetic flow $\frac{d\phi_{mag}}{dt}$ produced by the permanent magnet(s) and captured by the coil(s).

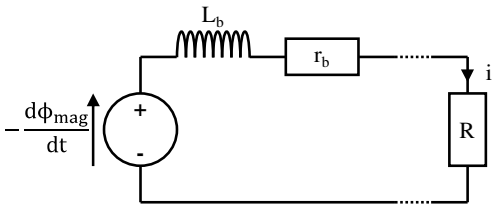

Figure 9: Schematic representation of an electromagnetic converter linked to a resistive load R.

By connecting our electromagnetic converter to an external load R, the following electrical equation (6) is obtained, with i being the current flowing from the harvester through the resistive load R:

$$\frac{di}{dt} + \left(\frac{r_b + R}{L_b}\right) i = -\frac{1}{L_b}\frac{d\phi_{mag}}{dt} \tag{6}$$

When the inductance of the converter is rather low (i.e. $L_b\omega_0 << r_b$), which will be our case experimentally, the corresponding electrical damping depends only on the relative position between the center of the magnet(s) and the center of the coil(s) (z) and can be written as:

$$c_{elec}(z) = \frac{\left(\frac{\partial \phi_{mag}}{\partial z}\right)^2}{r_b + R} \tag{7}$$

Finally, the "useful" electrical power P_{elec_use} dissipated in the resistive load depends on the electrical damping c_{elec}, the internal resistance r_b [36], the load R and the relative velocity between the magnet(s) and the coil(s):

$$P_{elec\_use}(z) = \frac{R}{r_b + R} \times c_{elec}(z) \times \Delta \dot{z}^2 \tag{8}$$

A classical approach to enhancing the output power of an electromagnetic harvester is thus to increase the variations of magnetic flux and especially the velocity between the coils and the magnets, as underlined in equation (8). For this reason, our electromagnetic harvester will be composed of a stack of small permanent magnets with alternative polarities instead of a single large magnet and will use various coils as described in [32]. Thus, N_a cylindrical permanent magnets, of radius R_a, height H_a (aspect ratio $AR = \frac{H_a}{2R_a}$), and magnetic remanence B_r will be considered. The permanent magnets are alternated and separated by cylinders of the same height as the magnets H_f=H_a to ensure the simple bonding of the magnets and include 2×Na coils of similar height H_a, as shown in Figure 10. This arrangement is used to maximize the spatial variation of the magnetic flux when the center of the permanent magnet stack is aligned with the center of the winding, thus maximizing the electrical power.

The air-gap will be noted e, $R_{b1}=R_a+e$ represent the inner radius of the coil(s), and R_{b2} the outer radius of the coil(s). Overall, the height of the permanent magnet stack is therefore equal to $H=(2N_a-1)H_a$.

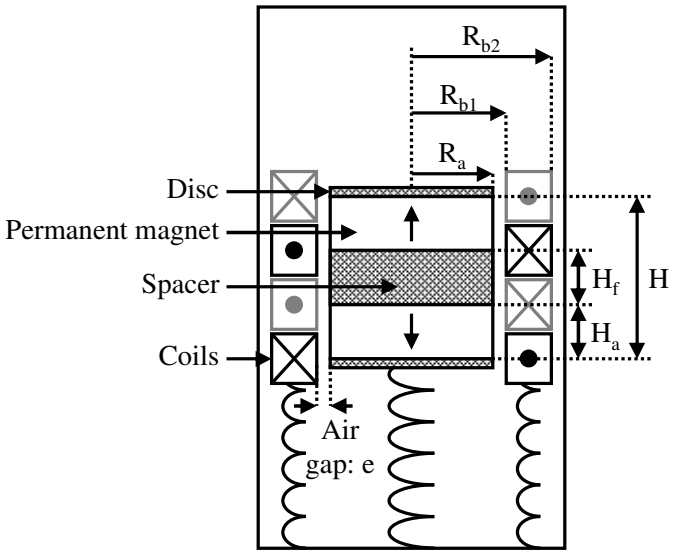

Figure 10: Example of a double winding electromagnetic converter (N_a=2, AR=0.33).

Simulations using the finite element software (Ansys®) were performed to estimate the variation of the magnetic flux. Compared to analytical modeling, these simulations are more precise as the edge effects of the permanent magnets are taken into account. Figure 11 presents the magnetic flux captured by thin coils ($R_{b1}\approx R_{b2}$), without an air-gap (e=0), as a function of the relative distance between the center of the permanent magnet stack and the center of the winding. The rest position (z=0) is the central position shown in Figure 11. It can be underlined that increasing the number of magnets (from N_a=1 to N_a=4) tends to reduce the spatial pseudo-period of the magnetic flux and its amplitude. However, it can be seen that the magnetic flux is cancelled at the equilibrium position of the magnet (z=0) while the spatial variation of the magnetic flux is maximal (zoom box in Figure 11). It may also be noted in Figure 11 that the positive effect of the number of magnets is limited regarding the maximization of the spatial variation of the magnetic flux, as the slope at z=0 increases from N_a=1 to N_a=2 permanent magnets and then remains almost constant for $N_a\geq 2$. Our final device will therefore be based on two permanent magnets. It is also apparent that the spatial variation of the magnetic flux is constant for small displacements around z=0, i.e. $\frac{\partial \phi_{mag}}{\partial z} = cte = \alpha$, leading to constant electrical damping.

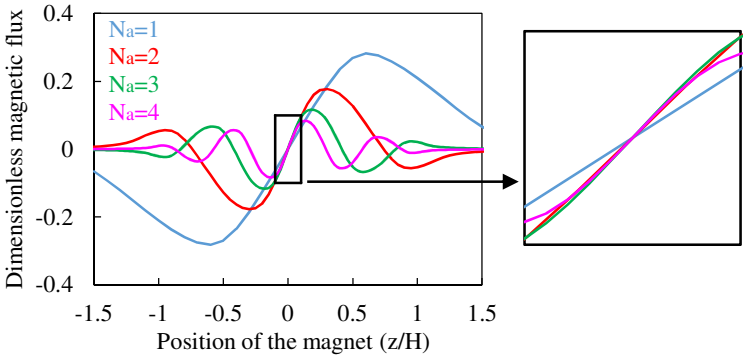

Figure 11: Effect of the number of magnets on the dimensionless magnetic flux $\left(\frac{\phi_{mag}}{N\pi {R_a}^2 B_r}\right)$ captured by an infinitely thin double winding ($\frac{H}{2Ra}$=1, e=0, $R_{b1}\approx R_{b2}$). Finite element simulations with Ansys®.

Finally, it is also possible to increase the magnetic flux captured from the first layers of the winding by adding different conveniently placed ferromagnetic parts. For example, substituting the non-magnetic spacers with soft iron spacers increases the spatial variation of the magnetic flux from 13% to 17%. Adding thin ferromagnetic outer discs on the permanent magnet stack (as illustrated in Figure 10) increases the spatial variation of the magnetic flux from 27% to 30%. Therefore, a configuration with

two permanent magnets, a soft ferromagnetic spacer, two outer discs and an air gap of 1mm made it possible to obtain the variation of the magnetic flux shown in Figure 12a. The parameters described in Table 1 were chosen. Increasing the thickness of the coils tends to increase the variation of the magnetic flux and the electrical damping c_{elec}, in agreement with equation (7).

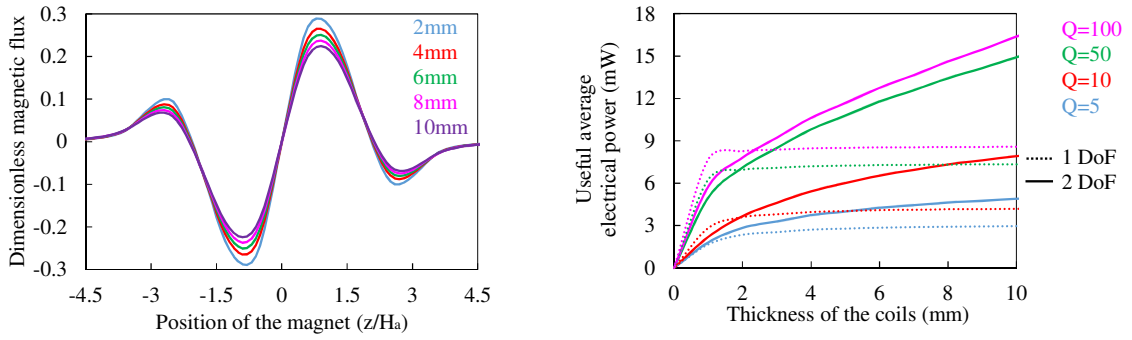

(a) (b)

Figure 12: (a) Variation of the dimensionless magnetic flux $\left(\frac{\Phi_{mag}}{N\pi {R_a}^2 B_r}\right)$ for different coil thicknesses. N is the number of turns of the coils. Finite element simulations with Ansys®. (b) Useful average electrical power vs coil thicknesses. H_a=20mm, R_a=17.5mm, B_r=1.35T, N_a=2, e=1mm. 1 DoF optimal frequency: f_{01}=33Hz. 2 DoF optimal frequencies: f_{01}=28Hz, Q=5: f_{02}=70Hz, Q=10: f_{02}=40Hz, Q=50: f_{02}=40Hz, Q=100: f_{02}=40Hz.

Figure 12b shows the effect of the coil thickness R_{b2}- R_{b1} on the average electrical power for different mechanical quality factors and an optimal frequency tuning, as described in section 2.1. For one DoF systems, increasing the thickness of the coils enabled increasing the electrical power up to a plateau reached for a coil thickness larger than 2mm. Indeed, as the thickness of the coils increased, the outer coils received less and less magnetic flux (as shown in Figure 12a), while the resistance of the coils r_b increased continuously, leading to lower electrical damping, according to equation (7) and thus to lower useful electrical power (equation (8)). For the two DoF system, Figure 12b shows that the electrical power increases fairly continuously as the thickness of the coils increases. Indeed, the result of amplifying the mass m_2 of the coils is to increase the associated inertial power and thus the useful electrical power. The contribution of the second degree of freedom therefore appears above a certain coil thickness value, approximately equal to 2-3mm, for all the mechanical quality factors.

3. Experiments and discussions

3.1 Final design of the harvester

Figure 13 shows a cross-sectional view of the final energy harvester which is composed of a stack of permanent magnets (N_a=2) and two pairs of coils, as deduced from the analytical optimization of the device. The two pairs of coils are located on an inner 3D printed cylindrical casing (Figure 14b) and a 3D printed 1mm-thick cylindrical outer casing is placed around the assembly (Figure 14c). Moreover, as our harvester is a parallel two DoF system, a specific spring named “double membrane spring” was designed. Two double membrane springs are fixed on both sides in order to connect the outer casing, the permanent magnet stack and the inner casing supporting the coils as shown in Figure 13. Finally, safety edges were added in order to restrict the displacement of each degree of freedom and avoid the plastic deformation of the membrane springs. The geometrical parameters of our harvester are summarized in Table 1.

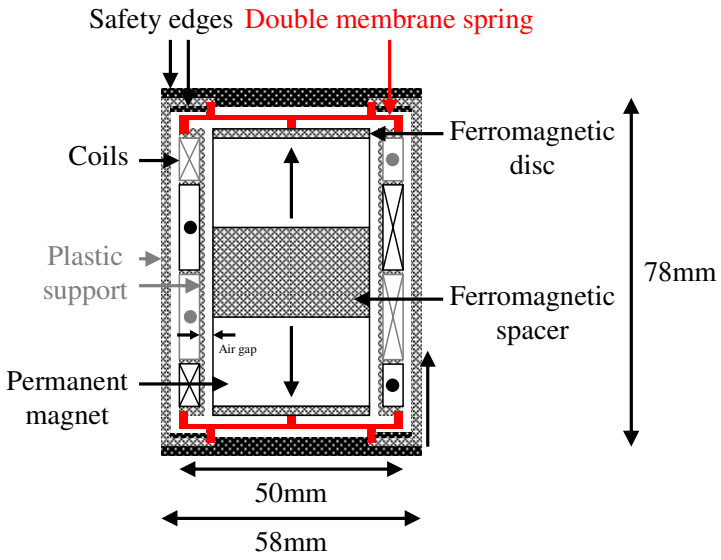

Figure 13: Cross-sectional view of the complete system.

(a) (b) (c)

Figure 14: Pictures of: (a) the permanent magnet stack (m_1=469g), (b) the winding (m_2=195g), (c) the complete assembly and one half of the SLA casing.

Table 1. Geometrical parameters of our harvester.

Number of permanent magnets N_a	2	Number of coils	4
Material	N42 Neodymium	Material	Copper wire
Radius of the permanent magnet R_a (mm)	17.5	Outer radius of the coils (mm)	25
Height of the permanent magnet H_a (mm)	20	Thickness of the coils (mm)	4.5
Radius of the spacer (mm)	20	Number of spires of the coils	1800
Height of the spacer (mm)	17.5	Diameter of the wire of the coils (µm)	315
Radius of the outer disc (mm)	17.5	Air gap (mm)	3
Height of the outer disc (mm)	2		

As described in section 2.1, frequency hopping occurs when optimizing the second resonance frequency dependent on the mechanical quality factor of the harvester. As the mechanical quality factors are difficult to control and strongly dependent on the manufacturing of the spring, the decision was taken to manufacture two different prototypes called P1 and P2, one adapted to low quality factors and the other to high mechanical quality factors. Both prototypes shared the same magnets and coils but the double membrane springs were slightly modified (thickness, number of sectors, angle formed by the sectors, etc.) to set the required resonance frequencies. The double membrane springs were designed using finite element software to obtain the first prototype P1 with resonance frequencies f_{01}≈28Hz and f_{02}≈70Hz, and the second prototype P2 with f_{01}≈28Hz and f_{02}≈40Hz. This double membrane spring was composed of three sectors for each spring (namely 2x3 sectors), themselves composed of concentric branches to ensure low stiffnesses (10-40N.mm^{-1}), as shown in Figure 15 and described more precisely in [37]. The springs (stainless steel 304) are amagnetic to prevent any attraction from the permanent

magnet stack. When assembling the harvester, the central ring (in blue on Figure 15) is screwed directly on the magnet stack, the median ring (in red on Figure 15) is glued to the outer casing and the outer ring (in green on Figure 15) is fixed to the inner casing supporting the coils. This type of design provides two non-bulky membrane springs (7.85cm^3 each) in a single piece, which could lead to lower manufacturing costs and a much simplified final assembly.

Figure 15: Picture of a double membrane spring developed for this application.

3.2 Test bench

Both prototypes (P1 and P2) were tested on a dedicated test bench (Figure 16a) capable of reproducing all the acceleration signals measured on the tram (Figure 3). An electrodynamic shaker (B&K LDS V408) drove a test platform on which the prototype harvester was clamped. A second shaker could have been used to simulate in-plane excitation as well as perturbations, but it was not used in the following results. Three piezoelectric charge accelerometers (B&K type 4393) were positioned on the test platform to compute the transfer function of the test bench and thus precisely reproduce the input signals measured on the real tram and apply them to the harvester in the frequency range 0-400Hz. For example, Figure 16b plots the PSD related to a trip between Europe-Université and Parilly-Université Hippodrome in Lyon.

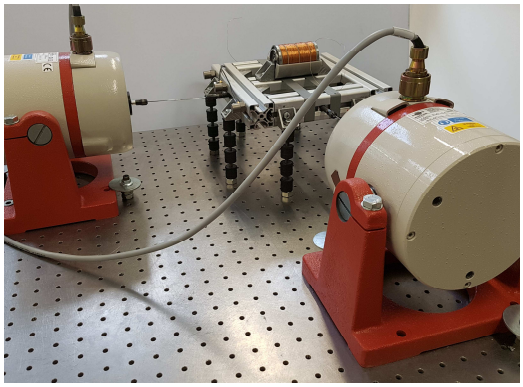

(a)

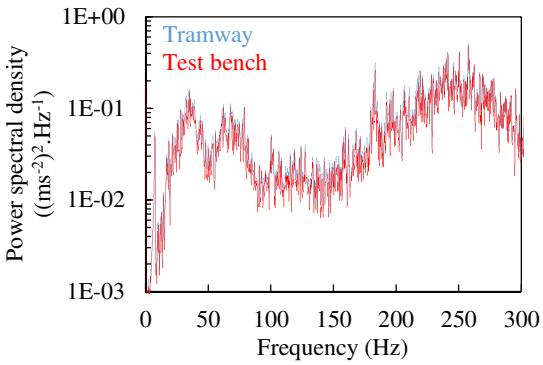

(b)

Figure 16: (a) Picture of the test bench used to test the harvesters. (b) Comparison of the PSD measured on the tram and replay on the test bench (for a trip between Europe-Université and Parilly-Université Hippodrome).

3.3 Preliminary experimental results

In the first step, both prototypes P1 and P2 were mechanically loaded with white noise on the test bench to identify the two natural resonance frequencies f_{01} and f_{02}, and the two mechanical quality factors Q_1 and Q_2 linked to the two DoF. All these parameters for the two prototypes are summarized in Table 2.

Table 2. Parameters linked to the two prototypes.

	P1 prototype	P2 prototype
m_1 (g)	471 (469+2)	471

m_2 (g)	214 (195+19)	214
m_{carter} (g)	38	38
m_{tot} (g)	710	710
f_{01} (Hz)	25.7	25.7
f_{02} (Hz)	62.6	40.2
Q_1	65	57
Q_2	30	95
r_b	56.5Ω	56.5Ω
L_b	36.5mH	36.5mH
c_{elec}*	2.26	2.49

It can be observed that the first resonance frequency was equal to 26 Hz experimentally instead of 28Hz theoretically, for both prototypes. The second resonance frequency was equal to 63Hz experimentally for P1 (instead of 70Hz) and 40Hz (as expected theoretically) for P2. These differences could mainly be explained by manufacturing inaccuracies, especially on the double membrane spring thickness which had a significant impact on the stiffness of the spring and thus on the resonance frequencies. Indeed, a variation of 10% was measured on the thickness of the springs. The average electrical power was recorded on various resistive loads from 10Ω up to 5000Ω. Figure 17a and Figure 18a show the average electrical power normalized by the square of the acceleration for both prototypes. Figure 17b and Figure 18b present the numerical results obtained by the two DoF model after the experimental identification of both mechanical quality factors (Q_1 and Q_2) and the resonance frequencies (f_{01} and f_{02}). The electrical damping c_{elec}, written in Table 2, was derived from the finite element calculations of the variation of the magnetic flux. Therefore, good correspondence between the numerical model and the measurements was obtained. This perfect fit validated our assumptions regarding the linearity of the springs and the electrical damping. Since the experimental mechanical quality factors ranged between 30 and 95 according to the prototype, it can be expected that prototype P2 performed better than P1 with real tram signals.

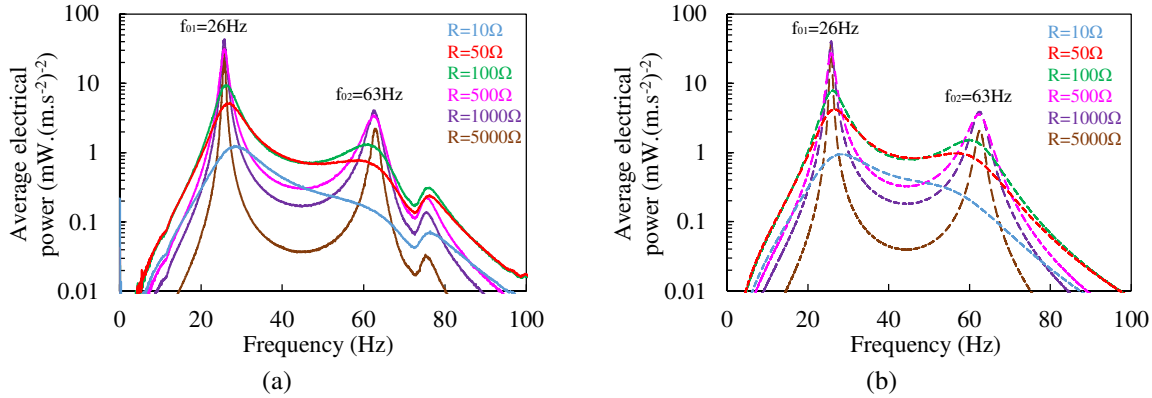

Figure 17: Transfer functions of prototype P1: (a) measurements and (b) numerical model after the experimental identification of f_{01}, f_{02}, Q_1 and Q_2.

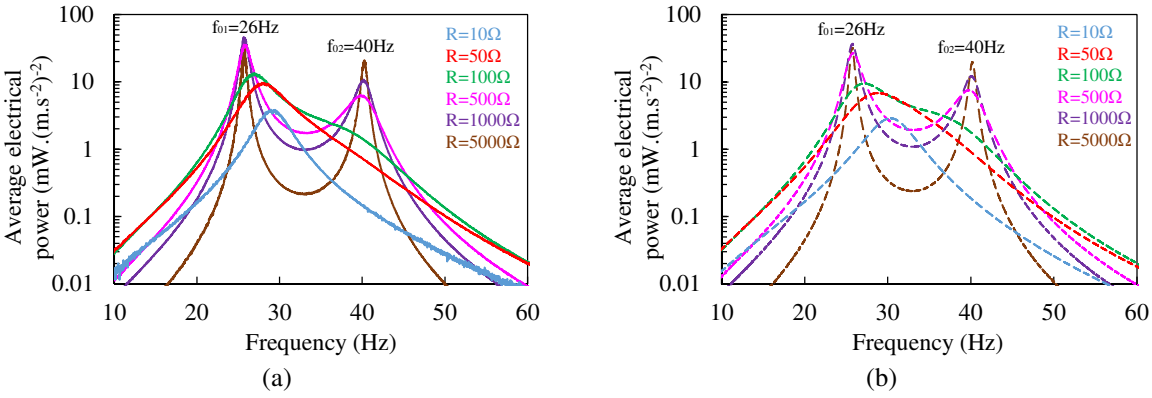

Figure 18: Transfer functions of prototype P2: (a) measurements and (b) the numerical model after the experimental identification of f_{01}, f_{02}, Q_1 and Q_2.

3.4 Performances with real tram signals

Figure 19a and Figure 19b show the measured electrical power averaged over all the trips and the measured stored electrical energy, respectively. The measurements are in good agreement with the numerical model (dashed line in Figure 19), thus validating the mechanical equations, the magnetic flux calculated by FEM and the different hypotheses of linearity (for both mechanical and electrical damping).

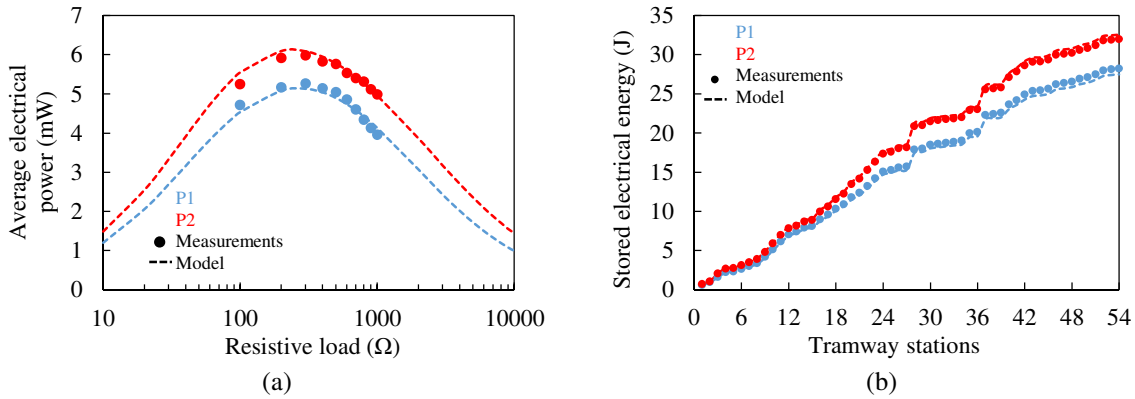

Figure 19: (a) Electrical power averaged over 179 trips between different stations and (b) the stored electrical energy (R=300Ω). In both cases, the measurements were performed on the test bench.

In Figure 19a, it can be seen that the optimal resistive load is close to R_{opt}=300Ω for both prototypes, which is significantly lower than the optimal resistive load for a sinusoidal excitation with a frequency of 26 Hz (Figure 17a and Figure 17b). As the winding resistance is equal to r_b=56.5Ω, this means that R_{opt}/r_b=5.3. For this optimal resistive load, the average electrical power is equal to 5.7mW (8.0mW.kg^{-1}) and 6.5mW (9.2mW.kg^{-1}) for prototypes P1 and P2, respectively. As the average time between two stations is approximatively 110 seconds, this implies an average stored electrical energy of 700mJ per station on the optimal load of 300Ω (Figure 19b).

The average power levels (5.7mw and 6.5mW for both prototypes) are quite sufficient to supply low consumption systems for structural health monitoring (SHM) such as accelerometers or temperature sensors [38]. For our tramway application, these results on energy harvesting capability highlight the future possible development of embedded health monitoring systems. Each sensor node of the SHM network could be energetically autonomous with a scavenger co-located with the sensor, the electronic and the communication systems. This SHM system could be simply plug into the structure to monitor, with a relative low added mass compared to the total structure's mass (here the bogie) and with no electrical wire between the SHM system and the power or control units of the tramway. Our harvester is thus a first step toward the development of a complete node leading to SHM systems able to sense the health of the tramway or the rails which could induce several benefits. Indeed, instead of having a scheduled maintenance every x km, the operator can act in prevention or when it is really necessary which allows significant economic gains and lower maintenance periods. Moreover, as the tramway is monitored, mechanical failures are detected and prevented which improves the system reliability and also the comfort of the passengers.

However, adding a second DoF in our harvester involves the use of a double membrane spring specifically dedicated to this application which could complicate the device assembly and can constitute a disadvantage for a potential commercialization of the product.

By way of comparison, the commercial device from Perpetuum (one DoF, f_{01}=100Hz) which was tested directly on the bogie of a tram in Lyon produced an average electrical power of 750µW.kg^{-1}. Similarly, the modelD from Revibe (one DoF, f_{02}=75Hz) produced an average electrical power of 1.77mW.kg^{-1}. These levels of harvested power are very low but can be partially explained by the fact that the two resonance frequencies of the two commercial devices (Perpetuum and Revibe) were not adapted to the vibratory environment of a tram. However, it is difficult to compare our results with the other devices of the state of the art given that none of them have been properly tested with real railway

excitation. The literature on inertial vibration energy harvesters for train and tram applications are summarized and compared with our prototypes in Table 3.

Table 3. Inertial vibration energy harvesters of the state of the art.

Reference	Model	RMS acceleration ($m.s^{-2}$)	Resonance frequency (Hz)	Size	Added mass (g)	Type	Electrical power (mW)
[18] and [19]	Clamped-clamped beam	10	300	$3.6\times2.1cm^2$	1.45	Piezo	0.3
[20]	Clamped-free beam	1.96	8.56	$3.5\times6.1cm^2$	36.62	Piezo	0.098
[21]	Magnetic levitation		3-5	$15\times12.5\times9.5cm^3$	164	Emag	
[22] and [23]	Clamped-free beam	2.06	65.2	$5.1\times3.2cm^2$	4	Piezo	0.74
[24]	Clamped-free beams	4.91	20	$24\times6.4\times3.2cm^2$	4	Piezo	24×0.256
[25]	Clamped-free beam	0.31	90	$6.9\times3.7cm^2$	38	Piezo	
[26]	Membrane	9.81	150	$3\times\pi\times2^2cm^2$	80-100	Piezo	21.4
[27]	Clamped-free beam STS 304	9.81	51.5	$8.8\times5.4\times4.7cm^3$	5.77	Emag	0.28
	Clamped-free beam Invar42	9.81	51.5	$8.8\times5.4\times4.7cm^3$	5.77	Emag	1.19
[28]	Clamped-free beam	49.05	7		60	Piezo	0.610
[29]	Mechanical spring	29.4	6	$10\times7\times6cm^3$	50	Emag	15
	Magnetic levitation	4.91-9.81	3-7	$24\times14\times21\ cm^3$	50	Emag	5.56
[30]	Clamped-free beam + pendulum	0.5	3.8	$33.7\times10.8cm^2$		Piezo	0.01268
Perpetuum		4.91	25-120	$\pi\times3.5^2\times6.5cm^3$	1030	Emag	27.5
Revibe	ModelA	29.4	15-100	$15.5\times5.3\times1.7cm^3$	300	Emag	150
	ModelD	4.91	15-100	$\pi\times1.6^2\times6.1cm^3$	120	Emag	40
Flexous	Hiper-D	49.05	35	$\pi\times1.7^2\times5.5cm^3$	82	Emag	90
Arveni		4.91	50			Piezo	200
MicroStrain	PVEH	14.72	1000	$\pi\times2.2^2\times4.3cm^3$	185	Piezo	30
	MVEH	1.96	20	$\pi\times2.9^2\times6.5cm^3$	216	Emag	4
Ferrosolutions	VEH-460	0.98	60		430	Emag	5.2
Our work	**P1**		**28 and 63**	**$\pi\times2.9^2\times7.8cm^3$**	**471+214**	**Emag**	**5.7**
	P2		**28 and 40**	**$\pi\times2.9^2\times7.8cm^3$**	**471+214**	**Emag**	**6.5**

Finally, it should be borne in mind that the output electrical power of our prototypes could be increased if the manufacturing was well controlled. Indeed, the experimental resonance frequencies differed from those expected in theory and obtained from our optimization process. Also, the air gap was set to 3mm in our prototypes, which remains a high value. With appropriate resonance frequencies and a small air gap (1mm), a gain of 1.5 was expected on the output electrical power, leading to an output power close to 10mW for a prototype of almost the same size as the commercial one though lighter.

Conclusions

An innovative two degree-of-freedom energy harvester used in the context of tram applications was designed. The originality of our optimization relies on a complete mixed analytical/numerical modelling using real input vibration signals which is quite unique. With our complex wide band vibratory environment with two predominant frequencies, it was shown that the two resonance frequencies of the harvester must not be equal to the two predominant frequencies of the input signal which differed considerably in comparison to the one DoF device or to classic optimization done for simple input signals such as sinus. Frequency hopping dependent on the mechanical quality factors linked to the two DoF occurred. For a high mechanical quality factor, the resonance frequencies must be closer to the predominant frequencies which was not the case for low mechanical quality factors. As a result, the harvested electrical power can be improved from 70% to 100% just by adding a second DoF, confirming the interest of a two DoF system compared to a one DoF. In this paper, the optimization has been achieved in the context of tram applications, but the method can also be applied to any vibratory signals in transport or energy applications (car, engine, industrial tool, plane…). Our proposed optimization is a powerful tool for industrial applications as it can be easily tunable and adaptable to any kind of input

vibration spectrum and can compute the amount of harvested energy in real conditions. However, a large number of data are necessary and must be collected in real operating conditions which could be expensive and/or time consuming

Two prototypes were designed, manufactured and tested on a test bench with real signals to validate our optimization. The average electrical power of the best prototype (P2) was equal to 6.5mW, which was close to the results obtained by numerical simulation and quite enough to supply sensors for structure health monitoring applications. Finally, to increase the electrical power produced by the harvester, further investigations should explore the membrane spring manufacturing and assembling methods which had a strong impact on the mechanical quality factors of the structure.

Acknowledgements

The authors would like to thank the French National Agency for the Environment ADEME for funding this project (MAVICO), and Keolis for giving us access to a tram and allowing us to perform experiments on the railway infrastructure of Lyon.

References

[1] C. A. Nelson, S. R. Platt, D. Albrecht, V. Kamarajugadda, and M. Fateh, Power harvesting for railroad track health monitoring using piezoelectric and inductive devices, Active and passive smart structures and integrated systems (2008).
[2] S. E. Hansen, A. Pourghodrat, C. A. Nelson, and M. Fateh, On-track testing of a power harvesting device for railroad track health monitoring, Health monitoring of structural and biological systems (2010).
[3] K. J. Phillips, C. A. Nelson, and Mahmood Fateh, Simulation and control system of a power harvesting device for railroad track health monitoring, Health monitoring of structural and biological systems (2011).
[4] A. Pourghodrat, C. A. Nelson, K. J. Phillips, and M. Fateh, Improving an energy harvesting device for railroad safety applications, Active and passive smart structures and integrated systems (2011).
[5] J. J. Wang, G. P. Penamalli, and L. Zuo, Electromagnetic energy harvesting from train induced railway track vibrations, Mechatronics and embedded systems and applications (2012).
[6] J. Wang, T. Lin, and L. Zuo, High efficiency electromagnetic energy harvester for railroad application, International design engineering technical conferences and computers and information in engineering conference (2013).
[7] T. Lin, J. Wang, and L. Zuo, Energy harvesting from rail track for transportation safety and Monitoring
[8] A. Bendekar, P. Dixit, U. Patel, N. Solanki, and A. Patil, Energy harvesting systems design for railroad safety, International journal of recent scientific research (2016).
[9] X. Zhang, Z. Zhang, H. Pan, W. Salman, Y. Yuan, and Y. Liu, A portable high-efficiency electromagnetic energy harvesting system using supercapacitors for renewable energy applications in railroads, Energy conversion and management (2016).
[10] T. Lin, J. Wang, and L. Zuo, Energy harvesting from rail track for transportation safety and monitoring (2014).
[11] C. Nagode, M. Ahmadian, and S. Taheri, Motion-based energy harvesting devices for railroad applications, Joint rail conference (2010).
[12] C. A. Nelson, A. Pourghodrat, and M. Fateh, Energy harvesting from vertical deflection of railroad track using a hydraulic system for improving railroad track safety, International mechanical engineering congress and exposition (2011).
[13] A. Pourghodrat and C. A. Nelson, A system for generating electricity using the passage of train wheels for improving railroad track safety, International design engineering technical conferences and computers and information in engineering conference (2012).
[14] A. Pourghodrat, C. A. Nelson, S. E. Hansen, V. Kamarajugadda, and S. R. Platt, Power harvesting systems design for railroad safety, Institution of mechanical engineers, part F : Journal of rail and rapid transit (2014).
[15] C. A. Nelson, Regenerative power for track health monitoring.
[16] Y. Tianchen, Y. Jian, S. Ruigang, and L. Xiaowei, Vibration energy harvesting system for railroad safety based on running vehicles, Smart materials and structures (2014).
[17] J. Wang, Z. Shi, H. Xiang, and G. Song, Modeling on energy harvesting from a railway system using piezoelectric transducers, Smart materials and structures (2015).
[18] M. Wischke, G. Biancuzzi, G. Fehrenbach, Y. Abbas, and P. Woias, Vibration harvesting in railway tunnels, Micro and nanotechnology for power generation and energy conversion applications (2010).
[19] M. Wischke, M. Masur, M. Kroner, and P. Woias, Vibration harvesting in traffic tunnels to power wireless sensor nodes, Smart materials and structures (2011).
[20] G. De Pasquale, A. Soma, and F. Fraccarollo, Piezoelectric energy harvesting for autonomous sensors network on safety-improved railway vehicles, Institution of mechanical engineers, part C: Journal of mechanical engineering science (2011).

[21] G. De Pasquale, A. Soma, and N. Zampieri, Design, simulation, and testing of energy harvesters with magnetic suspensions for the generation of electricity from freight train vibrations, Journal of computational and nonlinear dynamics (2012).
[22] J. Li, S. Jang, and J. Tang, Design of a bimorph piezoelectric energy harvester for railway monitoring, Journal of the Korean society for nondestructive testing (2012).
[23] J. Li, S. Jang, and J. Tang, Optimization of piezoelectric energy harvester for wireless smart sensors in railway health monitoring, Sensors and smart structures technologies for civil, mechanical, and aerospace systems (2013).
[24] J. Ortiz, P. M. Monje, N. Zabala, M. Arsuaga, J. Etxaniz, and G. Aranguren, New proposal for bogie-mounted sensors using energy harvesting and wireless communications, Institution of mechanical engineers, part F : Journal of rail and rapid transit (2013).
[25] D. Song, C. H. Yang, S. K. Hong, S. B. Kim, M. S. Woo, and T. H. Sung, Study on application of piezoelectricity to Korea train express (KTX), Ferroelectrics (2013).
[26] W. Wang, R. J. Huang, C. J. Huang, and L. F. Li, Energy harvester array using piezoelectric circular diaphragm for rail vibration, Acta mechanica sinica (2014).
[27] H. Park and J. Kim, Electromagnetic induction energy harvester for high-speed railroad applications, Precision engineering and manufacturing-green technology (2016).
[28] M. Y. Gao, P. Wang, Y. Cao, R. Chen, and C. Liu, A rail-borne piezoelectric transducer for energy harvesting of railway vibration, Journal of vibroengineering (2016).
[29] M. Gao, P Wang, Y. Cao, R. Chen, and D. Cai, Design and verification of a rail-borne energy harvester for powering wireless sensor networks in the railway industry, Transactions on intelligent transportation systems (2016).
[30] J. Y. Cho, S. Jeong, H. Jabbar, Y. Song, J. H. Ahn, J. H. Kim, H. J. Jung, H. H. Yoo, and T. H. Sung, Piezoelectric energy harvesting system with magnetic pendulum movement for self-powered safety sensor of trains, Sensors and actuators A : Physical (2016).
[31] C. B. Williams, and R. B. Yates, Analysis of micro-electric generator for microsystem, Sensors and Actuators A: Physical (1996).
[32] M. Geisler, S. Boisseau, M. Perez, P. Gasnier, J. Willemin, I. Ait-Ali, and S. Perraud, Human-motion energy harvester for autonomous body area sensors, Smart materials and structures (2017).
[33] M. Perez, S. Chesné, C. Jean-Mistral, K. Billon, S. Bouvet, and C. Clerc, A two degree-of-freedom electromagnetic vibration energy harvester for the railway infrastructure monitoring, Smart materials, adaptive structures and intelligent systems (2018).
[34] M. Perez, S. Chesné, C. Jean-Mistral, K. Billon, S. Bouvet, and C. Clerc, Optimization of a two degree-of-freedom vibration energy harvester for a dual-frequency excitation, Recent advances in structural dynamics (2019).
[35] S. J. Orfanidis, Introduction to signal processing, Rutgers University (2010).
[36] S. Zhou, C. Jean-Mistral, and S. Chesné, Influence of internal losses on optimization of electromagnetic energy harvesting, Smart materials and structures (2017).
[37] M. Perez, K. Billon, S. Chesné, C. Jean-Mistral, S. Bouvet, and C. Clerc, Design of a double spring membrane for a two degree-of-freedom electromagnetic vibration energy harvester, Surveillance Vibration Shocks and Noise (2019).
[38] M. Perez, S. Boisseau, M. Geisler, P. Gasnier, J. Willemin, G. Despesse and J. L. Reboud, Aeroelastic flutter energy harvesters self-polarized by triboelectric effects, Smart materials and structures (2017).